Prolonged ocular exposure leads to retinal lesions in mice

Brent A. Bell[a,*], **Vera L. Bonilha**[a,b], **Stephanie A. Hagstrom**[a,b], **Bela Anand-Apte**[a,b], **Joe G. Hollyfield**[a,b], **Ivy S. Samuels**[a,c]

[a]Cole Eye Institute/Ophthalmic Research, Cleveland Clinic, Cleveland, OH, United States

[b]Cleveland Clinic Lerner College of Medicine of Case Western Reserve University, Cleveland, OH, United States

[c]Louis Stokes Cleveland VA Medical Center, Cleveland, OH, USA

Abstract

Retinal lesions in the posterior pole of laboratory mice occur due to native, developmental abnormalities or as a consequence of environmental or experimental conditions. In this study, we investigated the rate and extent of retinal lesions as a result of prolonged ocular exposure following general anesthesia. Following experimental preparation induction procedures (EPIP) involving general anesthesia, mydriasis/cycloplegia, and topical anesthesia to the cornea, two ocular recovery conditions (protected and unprotected) were tested within two different animal recovery chambers (open or closed). The anterior and posterior poles were evaluated for the development of retinal lesions using digital color photography, scanning laser ophthalmoscopy, and spectral-domain optical coherence during anesthesia recovery and up to 2.5 months thereafter. In some mice, electroretinograms, histological and immunohistological evaluations were performed to assess functional and structural changes that accompanied the retinal lesions detected by *in vivo* imaging. Our data suggests that prolonged ocular surface exposure to circulating ambient room air leads to significant anterior and posterior segment ocular complications. The most abundant, semi-reversible complication observed was the development of lesions in the outer retina, which had a 90% probability of occurring after 45 min of exposure. The lesions mostly resolved short-term, but functional and imaging evidence suggest that some perturbations to the outer retina may persist one or more months following initial development.

Keywords

---

1. Introduction

The laboratory mouse (*Mus musculus*) has been used for over a century in vision research (Pinto et al., 2008) and is a preferred animal model in biomedical research (Gargiulo et al., 2012) (Krebs et al., 2017). During a 10-year tenure of *in vivo* ocular imaging sessions performed by a single operator, instances of "abnormal-looking" retina were observed in mice originating from over 15 principal investigators and collaborating laboratories. Some abnormalities were suspected to be naturally occurring, native problems associated with abnormal eye development (Bell et al., 2012), while others were introduced by vivarium lighting conditions (Bell et al., 2015). Interestingly, one unique abnormality was observed to occur across multiple strains, genotypes, research projects, and mouse treatments. Mice undergoing non-invasive experimental testing procedures involving general anesthesia exhibited similar-looking retinal abnormalities at a relatively low rate of occurrence. These abnormalities were not subtle and could be easily observed across multiple imaging platforms and modalities including color fundus photography, confocal scanning laser ophthalmoscopy, and spectral-domain optical coherence tomography. In some studies, anomalies were observed unilaterally and sometimes bilaterally in about 15–25% of subjects. Examples of procedures where mice developed abnormalities included laser-induced choroidal neovascularization, electroretinography, and various experimental treatments involving the administration of pharmaceuticals via subcutaneous or intraperitoneal injections, herein referred to as "primary" procedures. All occurrences shared a common trend in that they involved: 1) administration of an injectable agent for achieving general anesthesia, 2) administration of topical drops for pupil dilation and topical anesthesia,3) experimentation involving one of the aforementioned "primary" procedures, and 4) a post-session recovery period.

Baseline imaging was performed in some cohorts of mice before the start of the primary experiments to determine whether these abnormalities may be pre-existing (Bell et al., 2012). Abnormalities were not observed during the pre-screening sessions thus ruling out the possibility that these particular ocular complications were the result of preexisting conditions. However, the continuation of "primary" procedures using baseline-screened mice would again result in the development of retinal abnormalities. Following these episodes, it became clear that the conditions that mice were experiencing within the "primary" procedures resulted in the appearance of the retinal abnormalities.

We initially speculated that the abnormalities originate from pharmaceutical-induced exophthalmia. For decades, mice undergoing laboratory experiments have been administrated the popular drug combination Ketamine and Xylazine (KX) for general anesthesia (Arras et al., 2001; Gargiulo et al., 2012). Xylazine is an alpha-2 adrenergic receptor agonist that has been reported to induce exophthalmia in mice and rats, either systemically via injection, or topically by direct application to the eye (Calderone et al., 1986; Zeller et al., 1998). Mice anesthetized with another less popular small animal anesthesia agent, Sodium Pentobarbital (NaP), do not exhibit a similar proptosis effect. However, we observed that mice administered a minimal amount of phenylephrine after NaP developed exophthalmia similar to that of KX anesthetized animals. Phenylephrine, a routinely employed clinical mydriatic, is yet another adrenergic receptor agonist that acts in

a dose-dependent manner to induce proptosis on the mouse eye after being topically administered to the cornea (see Fig. S1).

Xylazine and phenylephrine have been routinely used in combination to prepare mice for ophthalmology-related experiments that require both anesthesia and mydriasis. Given that these drugs act similarly on the same general receptor and the eye as a whole by inducing proptosis, we sought to determine the possible consequences of using them in combination. We hypothesized that when used together excessive proptosis occurs secondarily to agonist-induced extraocular muscle relaxation and vasoconstriction, which may initiate retinal abnormalities.

We found that protecting the eye after experimental procedures mitigated ocular complications and that the drug-induced action involving proptosis was not the sole underlying trigger for the development of the observed retinal abnormalities. We further discovered that retinal abnormalities frequently occurred without careful post-procedural ocular care. The studies presented here will help (1) eliminate retinal abnormalities from all studies where they are not desired and could ultimately lead to confounding results, and (2) provide the vision research community with an attractive new acute model of localized outer retinal damage that can be non-invasively induced without the need for ocular surgery.

2. Methods

2.1. Animal subjects

Fifty wild type mice (n = 50) were obtained from the Cole Eye Institute animal vivarium under approved animal use protocols from the Cleveland Clinic Lerner College of Medicine Institutional Animal Care and Use Committee. The experimental procedures described herein were in accordance with the ARVO Statement for the Use of Animals in Ophthalmic and Vision Research. For Experimental Procedures 1 & 2, approximately half the mice were *Tulp1⁺/⁺* wild type littermates (n = 15, 2:1 male/female; Age: 10–39 wks) on a *C57BL/6J* background (Hagstrom et al., 1999) and the other half *C57BL/6J* (n = 16, 1:1 male/female; Age: 10–25 wks) (The Jackson Laboratory, Bar Harbor, ME). *Tulp1⁺/⁺* and *C57BL/6J* were reared independently within the same vivarium in two different rooms. Both tested negative for the Rd8 mutation of the Crb1 gene (Mattapallil et al., 2012) as previously described (Bell et al., 2015). Nineteen (19) additional *C57BL/6J* mice (1:2 male/female; Age: 8–10 wks) were used to demonstrate the differences between Sodium Pentobarbital (NaP) alone and Ketamine/Xylazine (KX) anesthesia combined with mydriatic/cycloplegia on exophthalmia.

All mice were housed on ventilated cage racks under standard vivarium conditions including a 14:10-h cyclic lighting, food and water ad libitum, corncob bedding, and cotton fiber nesting square and red-translucent enrichment hut. Experiments were performed over three months between September and November in 7 groups of mice. Typical vivarium ambient conditions ranged from 21 to 23 °C with 40–45% relative humidity. Typical procedure/imaging room ambient conditions ranged from 21 to 23 °C with a relative humidity of 25–45%. In late October, the relative humidity in the building dropped from 40–45% to 20–25% for both the animal vivarium and the experimental procedure and imaging rooms.

3. Experimental Induction of Retinal Lesions

3.1. Experimental Procedure 1: Uninterrupted recovery experiments

Experimental Procedure 1 is shown diagrammatically in Fig. S2. Mice were anesthetized using a mixture of Ketamine (80 mg/kg) and Xylazine (16 mg/kg) diluted in 0.9% saline to replicate routine experimental procedures requiring deep sedation (e.g., surgery, ocular imaging, electroretinograms, drug injections, laser-induced choroidal neovascularization induction). Within minutes of sedation, mydriasis/cycloplegia and topical anesthesia was induced by administering single drops of 2.5% phenylephrine (Akorn Inc., Lake Forest, IL, USA), 0.5% proparacaine, 1% tropicamide, and 1% cyclopentolate (Bausch and Lomb, Tampa, FL, USA), applied consecutively to the cornea. The process of inducing general anesthesia, mydriasis/cycloplegia, and topical anesthesia will herein be referred to as an Experimental Preparation Induction Procedure (EPIP). Approximately 1–2 min later, right (OD) eyes were protected by receiving a liberal dose of PuraLube Vet Ointment (Dechra Veterinary Products) used in conjunction with an ocular eye shield (Bell et al., 2014) whereas left (OS) eyes remained unprotected for the duration of the experiment.

Mice were placed into one of two acrylic containment devices for recovery, herein referred to as the "open" and "closed" chambers. Both chambers (Surgivet V711801, Smiths Medical, Dublin, OH, USA) were placed directly atop a heated hard pad connected to an Android Medical Heat Therapy Pump (Braintree Scientific, Braintree, MA, USA). The open and closed chambers were exposed or isolated to the ambient room environment, respectively. Environmental temperatures and relative humidity were documented using an indoor/outdoor digital thermometer and digital volt/temperature meter (Extech Instruments, Waltham, MA) with a Type T thermocouple. High relative humidity was maintained in the closed chamber by placing a moist paper towel on the bottom in addition to percolating dry compressed air through a custom-fabricated nebulizer. An appropriately sized silicone finger matt (Ambler Surgical, Exton, PA) was placed on top of moist paper towels to prevent mice from aspirating water condensate. Mouse body surface temperatures were measured in the open and closed chambers by placing a Type T thermocouple between the mouse abdomen and Plexiglas bottom or atop a layer of paraffin film placed over the finger matt, respectively. Mice were permitted to recover uninterrupted until regaining consciousness as assessed by evidence of mobility. The approximate time required for recovery was documented individually for each mouse.

3.2. Experimental Procedure 2: Interrupted recovery experiments

Experimental Procedure 2 is shown diagrammatically in Fig. S3. Eight mice that did not develop retinal lesions in the uninterrupted experiments were recycled for use in the interrupted recovery experiments. In these experiments, mice were prepared as aforementioned albeit initially without ocular protection. Immediately post-EPIP, mice were placed into the open chamber and permitted to recover naturally from the effects of anesthesia until exposure durations of 25, 45, 65 or 75 min were reached. Exposed eyes were subsequently covered with ointment and eye shields upon completion of the exposure duration process. Using a total of 8 mice, four eyes were tested at each exposure interruption time.

3.3. Ocular imaging

Various imaging modalities were employed to capture the ocular changes occurring to both the anterior and posterior segments. Images were collected immediately following EPIP and for up to 1.5 h afterwards during the uninterrupted and interrupted recoveries. Animals were temporarily removed from their respective chambers, imaged and returned as quickly as possible typically within 2–3 min.

Follow-up imaging to assess for the presence or absence of retinal lesions was performed at 3 and 14-days post-EPIP. Images were collected as previously described (Bell et al., 2014). A small number of mice (n = 3) were followed for up 80 days post-EPIP (2.5 months) to assess whether lesions persist long-term.

3.4. Digital color photography

An Apple iPhone 6 + was used to capture the effects of ocular protection or exposure on eyes in both the open and closed recovery chamber conditions. Images were collected from each mouse under standardized conditions that included a front-facing photo collected from a fixed 4" distance with the following settings (50% zoom, HDR On, original color setting, no flash, autofocus frame positioned on mouse forehead). Overhead room lighting was neutral white (4000 K) LED room lighting and measured to be ~500 Lux at bench top level.

Examples of retinal lesions at 3 and 80 days post-recovery were also captured using a custom-made topical endoscope fundus imaging (TEFI) system previously described (Paques et al., 2007).

3.5. Confocal scanning laser ophthalmoscope (cSLO or SLO)

A model HRA2 SLO (Heidelberg Engineering, Franklin, MA) was used to collect retinal fundus photos using 6 imaging modes including Infrared reflectance (IR), Infrared Dark-field (IRDF), Infrared autofluorescence (IRAF), Blue autofluorescence (BAF), Red Free Dark-field (RFDF) and Sodium Fluorescein Angiography (FA). A 55° wide-field lens was used to collect images with the optic disk centrally located in addition to peripheral views of the various regional quadrants.

3.6. Spectral-domain optical coherence tomography (SD-OCT)

Anterior and posterior pole imaging was performed using a Bioptigen model SDOIS SD-OCT system (Leica Microsystems, Buffalo Grove, IL). A Bioptigen mouse bore objective lens with a 50° field of view (FOV) was used for posterior pole imaging with an estimated lateral FOV of ~1.5 mm. Imaging of the anterior pole was performed using a 1-inch telecentric lens with an *en face* FOV of 5 mm (azimuth) × 5 mm (elevation) × 3.2 mm (depth). Orthogonal B-scans of the anterior and posterior poles were collected using a radial volume scan (1000 A-scans/B-scan; 2 B-scans, 15 frames). For the anterior pole, scans were positioned just inferior and to the side of the corneal apex reflex to avoid capture of streak artifact from bright specular reflections. Images of the posterior pole were collected at the horizontal and vertical meridians with the optic disk centrally positioned. Additional images of peripheral regions were collected in order to capture retinal pathology examples as needed.

3.7. Electroretinograms (ERG)

Photopic and scoptic electroretinography was performed on *C57BL/6J* mice as previously described (Samuels et al., 2013). After overnight dark adaptation, mice were anesthetized with Ketamine (80 mg/kg) and Xylazine (16 mg/kg) diluted in 0.9% saline, the cornea was anesthetized with 1% proparacaine, and the pupils were dilated with 1% tropicamide, 2.5% phenylephrine, and 1% cyclopentolate. Mice were placed on a temperature-regulated heating pad throughout each recording session. Responses of the outer retina were recorded using an Espion E3 ColorDome full-field ganzfeld (Diagnosys, Lowell, MA) with Ag-AgCl cornea electrodes referenced to a needle electrode placed in the cheek of the mouse and a ground electrode in the tail. For scotopic ERG, ten steps of blue (445 nm) + green (520 nm) light flash stimulus [-3.6 to 2.1 log candela (cd)·s/m^2] were presented in the dark in order of increasing flash strength, and the number of successive trials averaged together decreased from 20 for low-level flashes to 2 for the highest flash stimuli. The duration of the interstimulus interval increased from 4 s for low-luminance flashes to 90 s for the highest stimuli. The amplitude of the a-wave was measured 6.0 ms after flash onset from the prestimulus baseline. The amplitude of the b-wave was measured from the a-wave amplitude at 6.0 ms to the peak of the b-wave. Immediately following the dark-adapted strobe-flash stimuli a steady 20 cd/m^2 adapting field was presented in the ganzfeld bowl. After 10 min of light adaptation, photopic ERG recordings were obtained from strobe-flash stimuli (-1 to 2 log cd·s/m^2) superimposed on the adapting field. The amplitude of the b-wave was measured from the prestimulus baseline to the positive peak of the waveform. Statistical significance was determined by using a Multiple T-test corrected for multiple comparisons using the Holm-Sidak method with GraphPad Prism 6.0 software.

3.8. Data processing and analysis of imaging data

Images were exported from their respective imaging platforms to ImageJ 1.47b (Rasband 1997–2012) and Adobe Photoshop CS5 for processing and display. iPhone 6 + and SLO images were exported as JPEG and TIFF, respectively. Anterior and posterior pole SDOCT images were exported as.AVI files, opened in ImageJ, coregistered and averaged using StackReg/TurboReg plug-ins (Thévenaz et al., 1998). Graphical display of data and statistical analysis was accomplished using GraphPad Prism 6 (Graphpad Software, La Jolla, CA). Unless noted, all data are shown as mean ± standard deviation (SD). For all statistical tests, p values and adjusted p values are shown as actual written numerical values or asterisks as follows: ns = $p > 0.05$; *$p < 0.05$; **$p < 0.01$; ***$p < 0.001$; ****$p < 0.0001$.

iPhone images of ocular media opacities were analyzed using ImageJ by encircling the pupil and obtaining the mean red, green, and blue (RGB) values using the Measure RGB plug-in. Corneal specular reflections from overhead lighting were omitted from the analysis. RGB data (Fig. 1A and B) taken during the uninterrupted recovery experiments was converted to grayscale and analyzed to obtain mean opacity magnitude. An Ordinary One-way ANOVA with Sidak's Multiple Comparisons test was used for determining statistical significance.

IR- and RFDF- (Experimental Procedure 1) or IRDF-SLO (Experimental Procedure 2) images of the retina were analyzed for average lesion count or number (#), individual lesion size (area%), and collective or total, accumulative lesion area (Σarea%) for the available

image FOV. The available FOV for the uninterrupted recovery experiments included both central and peripheral SLO 55° views that included the superior, temporal, and nasal retinal regions, all of which were analyzed independently. Central view data (Fig. S4B) was analyzed with an unpaired two-tailed t-test with equal standard deviations. Peripheral view data (Fig. S4C) was analyzed with an ordinary One-way ANOVA with Tukey's multiple comparisons test.

The available image FOV for the interrupted recovery experiments was a Photoshop CS5 montage that combined central and peripheral views collected with the SLO 55° wide-field lens from all four retinal quadrants into a single image of the retina. Lesion count (#), individual lesion size (area%), and collective or total, accumulative lesion area (Σarea%) (Fig. 3A and B) obtained from the montaged images were analyzed using an ordinary One-way ANOVA with Tukey's multiple comparisons test.

SLO fundus image overlays were compiled using montaged images from the interrupted recovery experiments to better identify regions where lesions had the highest tendency to materialize. Using Photoshop, features of the retina were filled or traced, including the lesion involvement area (white), long-posterior ciliary arteries (red), optic disk (yellow), and vortex veins (blue) (Fig. 2B). Montaged images from three mice at exposure durations of 25, 45, 65, 75 min were overlaid and aligned in Photoshop using the long-posterior arteries and optic disks as landmarks. Once combined, the three individual montages from each time point were averaged to obtain a heat map of area overlap (Fig. 2B) showing the areas of highest (white) and lowest (black) tendencies for lesion formation.

Anterior segment SD-OCT data was analyzed for exophthalmia (e.g., proptosis), corneal thickness, anterior chamber depth, lens media opacity area, lens media opacity magnitude, and lens media opacity integrated density using ImageJ. Exophthalmia was measured from the cornea apex to the Medial Canthus. Cornea thickness and anterior chamber depth was measured from horizontal and vertical orthogonal B-scans through the central optical axis and averaged over ~10 frames. Lens media opacity data was obtained by encircling the opacity using a drawing tool and obtaining area, magnitude, and integrated density values in ImageJ. Area measurements of media opacities were converted from pixels to square millimeters by using a ruler for calibration of the B-scan image frame. Scatter plots were generated using pooled data from both uninterrupted and interrupted recovery experiments, and non-linear regression curve fits were performed to show mean ± 95% confidence interval bands. Data were fitted to a best-fit curve using R-squared values, which was usually a straight line or one-phase exponential decay (or association).

RGB values collected from the media opacity images (Fig. 7A) obtained during the interrupted recovery experiments were converted to CIE 1976 L*a*b* (Lab) color space (Fig. 7B–D) using an online conversion tool (Colormine.org). Lab hexadecimal color values were obtained using an online color picker tool (DavidJohnstone.net). MS Powerpoint was used to generate color bars and mouse pupil color replications using the obtained color values. Statistical significance for the mean Lab values measured was determined using an ordinary One-way ANOVA with Tukey's multiple comparisons test.

A Pearson correlation test was performed only for mice/eyes that developed retinal lesions. The test obtained correlation coefficients and p-values between collective lesion impact area and other measured variables that included a total of 236 total data points for exposure duration, exophthalmia, corneal thickness, anterior segment depth, lens media opacity area, magnitude and integrated density, and CIE L*a*b* values.

3.9. Histology

Eyes were enucleated and fixed by immersion in 2% paraformaldehyde, 2.5% glutaraldehyde and 5% $CaCl_2$ made in 0.1 M cacodylate buffer overnight at 4 °C and processed for epon embedding and imaging as previously described (Bonilha et al., 2015). Semi-thin sections were cut with a diamond histotech knife, collected on glass slides, and stained with toluidine blue. Slides were photographed with a Zeiss AxioImager.Z1 light microscope and AxioCam MRc5 camera.

3.10. Immunocytochemistry

Eyes were enucleated and fixed by immersion in 4% paraformaldehyde in PBS at 4 °C, quenched with 50 mM NH_4Cl for 30 min and then infused successively with 10% and 20% sucrose in PBS, and finally Tissue-Tek "4583" (Miles Inc., Elkhart, IN). Cryosections (8 μm) were cut on a cryostat HM 505E (Microm, Walldorf, Germany) equipped with a CryoJane Tape-Transfer system (Leica Inc., Buffalo Grove, IL). For labeling, sections were washed to remove embedding medium, blocked in PBS supplemented with 1% BSA (PBS/BSA) for 30 min, and incubated with primary followed by secondary antibodies coupled to Alexa 488 or Alexa 595 and finally incubated with TO-PRO-3 for nuclear labeling (LifeTechnologies, Grand Island, NY) as previously described (Bonilha et al., 2015). A series of 0.3-μm *xy* (*en face*) sections were collected using a laser scanning confocal microscope (Leica TCS-SP8, Exton, PA) using the same acquisition parameters for each channel in the Leica confocal software LAS AF. Antibodies used included rhodopsin (clone B630N, from Dr. G. Adamus, Oregon Health and Science University, Portland, OR, 1:100), glucose transporter GLUT1 antibody (ab652, 1:200) and Glial fibrillary acidic protein (GFAP, Abcam ab10062, 1:100).

4. Results

4.1. Uninterrupted Recovery Experiment Results

Mean age of the mice in the closed chamber was 27 ± 5 weeks. Mean age of the mice in the open chamber was 32 ± 8 weeks. The age difference observed between chambers was not significant (unpaired two-tailed *t*-test). The open chamber ambient conditions had a temperature range of 21–23 °C and relative humidity of 40–45%. The closed chamber ambient conditions had a temperature range of 28–30 °C and relative humidity of 75–95%. No substantial deviations in relative humidity were observed during the course of these experiments, which occurred during the months of September through early October. At 1 h post-sedation, mouse abdominal surface temperatures were measured (mean ± SD) to be 32.6 ± 2.9 °C (n = 5) and 35.5 ± 0.8 °C (n = 7) for the open and closed chambers, respectively and not significantly different (unpaired two-tailed *t*-test).

Fig. 1 shows the results obtained from the Uninterrupted Recovery Experiments. Right eyes (OD) that were protected were noticeably absent of any visible evidence of media opacity regardless of the recovery chamber condition. In contrast, left eyes (OS) that experienced prolonged ocular exposure exhibited both visible and quantifiable differences in media opacity response. As discerned in the digital photographs (Fig. 1A & B; white arrows), mice recovering in the open (126.9 ± 21.9 grayscale or "GS" units) vs. closed (36.2 ± 11.5 GS units) chambers with unprotected eyes were significantly (P < 0.0001; unpaired two-tailed t-test) more prone to developing severe media opacities. All ocular media opacities resolved to insignificant levels following recovery (Fig. 1A & B) when the mice were re-evaluated for evidence of retinal lesions at 14 days post-EPIP. However, two mice from the open chamber with unprotected left eyes developed corneal ulcerations and microphthalmia that prevented retinal imaging assessment.

In two cohorts of wild-type mice tested, posterior pole imaging at 14-days post-EPIP revealed retinopathy-like lesions in 70% (7/10) and 75% (3/4) of eyes from $Tulp1^{+/+}$ and $C57BL/6J$ mice recovered in the open chamber, respectively. Collectively, 71% (10/14) of wild-type mice developed lesions after being under general anesthesia for 1.5 h (Fig. 1C). A comprehensive analysis of the SLO imaging data was performed for the Uninterrupted Recovery Experiments and provided in Figs. S4A–C. Lesions could be observed to a varying degree using the five native reflectance and autofluorescence SLO imaging modes (Fig. 1D[1–5]). Two mice, out of 10 affected, had visible lesions only after the camera head was panned to the peripheral retina (see Fig. S4B). SD-OCT imaging immediately following SLO revealed lesions confined to the outer retina and almost exclusively to the photoreceptor layer (Fig. 1E-bracket). Hypo- and hyper-reflective features visualized by SD-OCT within the SLO identified lesion boundaries resembled pathologies common to Age-Related Macular Degeneration such as Outer Retinal Tubulation (ORT) (Zweifel et al., 2009) and Reticulated Pseudodrusen (RPD) (Khan et al., 2016). Histology confirmed the presence of outer retinal pathology (Fig. 1F[2–4] & 1G[2–5]) in affected areas confined to the photoreceptor outer segments and RPE. Hyporeflective circular features observed by SD-OCT imaging were found to be atypical of ORTs and more similar to pseudo or subretinal cysts as no cells were encircling the vesicular void (Fig. 1F[2] & 1G[2–5]). Additional observations included evidence of displaced melanosomes or melanin pigment granules (Fig. 1F[2&4] – yellow arrows), a detached RPE cell or infiltrating sub-retinal inflammatory cell (Fig. 1F[3] - yellow arrows), and RPE hypo-pigmentation (Fig. 1F[4]-black arrowheads). GFAP immunohistochemistry revealed no gliosis or activated Müller glia within the inner retina over areas with sub-retinal cysts (see Fig. S5).

Electroretinograms performed on the $C57BL/6J$ cohort one-month post-EPIP demonstrated that functional changes were correlated with the mice recovered without ocular protection in open chambers (Fig. S6). In Fig. S6A, the a-wave amplitude of mice without protection in open chambers is significantly smaller than those recovered with ocular protection. Similarly, the b-wave is significantly smaller in response to high flash stimuli (Fig. S6C). There is also a trend toward smaller light-adapted responses in mice recovered without protection in open chambers as compared to mice with ocular protection (Fig. S6E). In contrast, mice that underwent unprotected recovery, but in closed chambers, did not display

significant reductions in a- and b-wave amplitudes (Figs. S6B and S6D) or in light-adapted response (Fig. S6F).

4.2. Interrupted Recovery Experiment Results

In late October the ambient outdoor temperatures began to cool, which subsequently caused a reduction in ambient relative humidity in the vivarium and laboratories, both of which are housed within the same building. Although the indoor ambient temperature remained the same (21–23 °C) the relative humidity within the building dropped from 40–45% to 25–30% for mice undergoing Experimental Procedure 2. Despite this difference, abdominal surface temperatures (31–36 °C; n = 4) remained similar to those measured in the open chamber of Experimental Procedure1.

Two groups of *Tulp1*^{+/+} mice underwent a second episode of EPIP, with interrupted ocular protection occurring at 25, 45, 65, or 75 min. All mice were evaluated for retinal lesions three days post-EPIP. IRDF-SLO images from the retinas of affected and unaffected mice are shown in Fig. 2A. Montaged views of central and peripheral retina are shown with an approximate 110° FOV (55° × 2) taken from the horizontal and vertical meridians. At 3-days post-EPIP, lesions appear as dark areas relative to the normal background by IRDF-SLO imaging. Qualitatively it can be observed that the lesion number and area expand with increasing exposure duration. At 25 min mice had not developed any retinal lesions. After 45 and 65 min, 75% (3/4) of mice developed retinal lesions. At 75 min, 100% of the mice that could be imaged (3/3) had retinal lesions while the remaining mouse that could not be assessed had irreversible ocular damage in the form of microphthalmia secondary to an ulcerated cornea.

Mean overlays pinpoint areas of the retina that were vulnerable to lesion development (Fig. 2B). After 45 min of exposure, it is apparent that lesions are forming in the superior-nasal and inferior-temporal regions. At 65 min, lesions in the superior-nasal and inferior-temporal regions expand in coverage with an additional dominant location in the superior-temporal region emerging. Additional, smaller lesions appear in the nasal and superior regions at 65 min, and by 75 min, all observances increased in frequency, magnitude, and area, and have become widespread throughout the FOV.

Horizontal meridian SD-OCT B-scans from the same IRDF-SLO fundus image shown in Fig. 2A (Example No. 3 @ 75 min) are shown in Fig. 2C. A nasal region B-scan shows abnormal outer retina morphology through the middle of the lesion. Lesion severity was more pronounced at 3 days post-EPIP than 14 days (Fig. 2C vs. 1E). Both hyper- and hypo-reflective changes (Fig. 2C-nasal B-scan) appeared as hard or soft retinal exudates above subretinal pseudocysts or pyramidal "ghost" pseudodrusen, respectively (Khan et al., 2016). The temporal B-scan is taken at the edge of a lesion and thus absent of the cysts but shows a photoreceptor layer absent of normal morphology and axial displacement of the external limiting membrane and IS-OS/ellipsoid zone.

Fig. 3A graphically illustrates the quantified imaging data obtained from the interrupted recovery experiments. The total lesion area (Σarea %) is shown plotted and fitted with an exponential growth curve (Adj. R^2 = 0.98) in Fig. 3B. Mean total lesion area involvement

consistently increased in relation to the exposure time. Between 45 and 65 min, and 65 and 75 min, the total lesion area increased ~2.5 times. A One-way ANOVA indicated that the increasing trend in total lesion area was significant (p = 0.01) as well as the changes observed between 25 and 75 min (p = 0.008) and 45 and 75 min (p = 0.034). The mean number (#) of lesions increased with exposure time and was 0 ± 0, 4.3 ± 3.1, 6.3 ± 1.5, 8 ± 1 for 25, 45, 65, and 75 min, respectively. Average individual lesion size (area%), relative to the percentage of the montaged FOV, was 0 ± 0, 0.9 ± 0.6, 1.8 ± 0.9, 3.9 ± 2.6 for 25, 45, 65, and 75 min, respectively. For reference, the average size of the optic disk for the twelve fundus montages shown in Fig. 2A is ~0.24% of the montaged SLO FOV. Thus, the mean individual retinal lesion sizes calculated were on average 3.75, 7.5 and 16.3 times larger than the optic disk for 45, 65, and 75 min exposure times when observed by IRDF-SLO imaging at 3-days post-EPIP. A sigmoid response curve was generated (Fig. 3C) for mice with eyes that were unprotected and recovered in the open chamber that subsequently developed retinal lesions post-EPIP. The primary abscissa shown in Fig. 3C corresponds to the proportion of mice per group found with retinal lesions relative to mean exposure duration time for each of those groups. The secondary abscissa in Fig. 3C shows the estimated probability of lesion development relative to exposure time after fitting the data with a sigmoid curve (Adj. $R^2 = 0.84$). The effective dosage time estimated for half of the animals to develop lesions (ED_{50}) was 37.8 min.

4.3. Extended follow-up of exposure-induced retinal lesions

Mice observed with lesions at 3-days post-EPIP following a > 60-min recovery were monitored for up to 2.5 months to determine if the acutely-induced developments would resolve or persist long-term. Fig. 4 shows examples of lesions documented at 3-days post-EPIP and up to 80 days afterwards by SLO, TEFI and FA-SLO imaging. Fig. 4A demonstrates a prominent lesion observed by IRDF-SLO at 3-days post-EPIP that rapidly resolves to practically undetectable levels 14-days post-EPIP. Subtle changes persist at 14-days post, which appear as relatively small perturbations of hypo- or hyper-reflective spots, or variations in background intensity within the original lesion boundary relative to other unaffected areas of the image FOV. The spots slowly resolve over time to non-detectable levels by 80 days post when observed by IRDF-SLO imaging. The same lesion identified by IRDF (Fig. 4A) is shown by IR-, RFDF- and BAF-SLO in Fig. 4B. The IR reflectance image shows the lesion as a hypo-reflective area in the superior-temporal region that is not readily discernable 80 days post in the superior view; however to an experienced eye, some residual perturbations can be observed, such as punctate hyper- and hypo-reflective spots within the original lesion boundary. In contrast to the two IR imaging modes, blue light illumination imaging modes (RFDF and BAF) showed more apparent features at 80 days post. The RFDF and BAF imaging example suggest an outer retina still actively undergoing modification or repair from the original insult as hyper-reflective and/or autofluorescent features can be still be visualized in these images at 80-days post-EPIP.

The same mouse underwent TEFI imaging and SLO angiography to show the appearance of the lesions using visible-light fundus photography and for the presence of sodium fluorescein leakage at the previously documented lesions sites (Fig. 4C & D). TEFI showed the lesion areas as reddish hue in color suggesting visualization of the underlying

choriocapillaris and circulating erythrocytes (Fig. 4C). Additional TEFI images of lesions a few days post-EPIP are provided as supplemental materials for comparison to the mature lesion shown (Fig. 4C) and demonstrate that recently induced lesions have a reflective white appearance (Fig. S7) at 3-days post-EPIP. FA-SLO of the camera focus trained on the RPE showed irregular fluorescence patterns in the superior-nasal and superior-temporal regions relative to the surrounding areas (Fig. 4D). These regions of atypical visualization correspond well to the retinal lesions detected using TEFI and native reflectance/ autofluorescence SLO imaging modes that could indicate fluorescein uptake or leakage by the RPE or trans-RPE visualization of the circulating fluorescein within the choriocapillaris. Sodium fluorescein demarcation was no longer evident when the camera focus was repositioned to image the deep vascular capillary plexus of the retina further indicating that the defect is isolated to the distal region of the outer retina.

4.4. Anterior segment dynamics following EPIP

Imaging data collected in mice post-EPIP recovering from the acute effects of sedation was also analyzed to investigate what changes occur to the various entities within the anterior segment. Fig. 5 shows the anterior segment changes observed by SD-OCT in mice recovered in the open (Fig. 5A) and closed (Fig. 5B) chambers with eyes that were protected or left unprotected during the recovery period. Similar to the observations made in Fig. 1A, eyes that were protected (OD-open & closed chambers) showed very little change compared to eyes that were left unprotected (OS-open & closed chambers). Unprotected eyes in either recovery chamber exhibited media opacities that persisted throughout the exposure time regardless of chamber recovery type. However, mice recovered in the open chamber had more severe changes to the anterior segment region than those being recovered in the closed chamber.

Fig. 5C & D shows the exophthalmia results which consistently increased (~7–10%) or decreased (~3%) for protected vs. unprotected eyes, respectively, regardless of recovery chamber condition. In the cornea (Fig. 5E & F), protected eyes showed moderate swelling as thickness increased by 15–20% regardless of recovery chamber condition. Unprotected eyes showed differences in corneal shrinkage trends between mice recovered in closed vs. open chambers. Mice recovered in the closed chamber (Fig. 5F) with unprotected eyes exhibited nominal corneal thinning (~7%) whereas mice recovered in the open chamber (Fig. 5E) showed substantially more by comparison (~33%). Moreover, mice in the open chamber (Fig. 5E) reached this level of change after only 20–25 min, which remained an asymptotic limit throughout the remainder of the recovery period. Changes in anterior chamber depth (Fig. 5G and H) were substantial for one condition, which was for mice recovered in the open chamber without ocular protection (Fig. 5G, OS-unprotected). Over the entire recovery period, this group of mice exhibited a 4-fold reduction in anterior chamber depth on average. In comparison, anterior chamber depths for the other three recovery conditions (Fig. 5G, OD-protected and Fig. 5H, OD-protected & OS-unprotected) showed nominal increases of only ~10%. No appreciable lens media opacities were identified (Fig. 5A and B, Fig. 5I and J) for the protected eyes of mice recovered in either the open or closed chambers. Lens media opacities of unprotected eyes showed qualitative differences between mice recovered in open vs. closed chambers (Fig. 5A and B). Integrated density measurements of the media

opacities showed that mice with unprotected eyes recovered in the open chamber developed more severe cataracts than mice with unprotected eyes recovered in the closed chamber by about ~20% (Fig. 5I and J). Fig. S8 separates the products of integrated density into the components of opacity area and magnitude independently to show the differences in media opacity development. From this figure, it can be observed that lens opacity area and magnitude reach asymptotes quickly at ~25 and ~15 min respectively, for mice recovered in the open chamber with unprotected eyes.

To better compare the changes observed in the anterior segment by SD-OCT, the first derivative was taken of the fitted data from Fig. 5C–J. Fig. 6 demonstrates that changes observed in the unprotected eyes of the mice recovered in the open chamber are more prominent than the other three treatment conditions. In terms of magnitude and duration, the anterior chamber depth has the most substantial and sustained rate of change over the post-EPIP recovery period. At 80 min post, anterior chamber depth changes persist and have yet to reach an asymptotic limit. The sustained changes occurring in the anterior chamber depth persisted longer than the smaller magnitude responses observed with corneal thinning and lens media opacity integrated density that reached asymptotes at ~25–30 min, well before the earliest documented lesion development at 45 min.

4.5. Visual recognition of ocular lens position by visual assessment of media opacity color and brightness

Fig. 7 shows color digital photos of the eyes of mice that were enrolled in the interrupted recovery experiments. Three examples per time point show the media opacities at 5, 25, 45, and 65 min post-EPIP. Fig. 7A demonstrates that the color and brightness of the media opacity changed over time with ocular exposure duration. The quantitative data extracted from the media opacity images is shown in Fig. 7C–E and presented in CIE L*a*b* color space. In L* (Fig. 7C), the brightness of the media opacity increased significantly with exposure time until reaching the 45–65-min data points where it appears to be approaching an asymptotic limit. In a* (Fig. 7D), the neutral green-red level observed at 5 and 25 min post-EPIP changes significantly to a more green hue at 45 (Adj. p = 0.0210) and 65 (Adj. p = 0.0127) minutes. With b* (Fig. 7E), the very slight blue hue observed at 5 min post-EPIP changes significantly more blue at 25 min (Adj. p < 0.0001), then significantly returns to the original baseline level observed at 5 min for the 45 (Adj. p < 0.0001) and 65 (Adj. p < 0.0001) minute data points.

To determine whether the mean CIE L*a*b* values obtained accurately represented the digital photos; a color rendition was generated for the four-time points evaluated. Shown below the representative media opacity photos in Fig. 7A are the color renditions (Fig. 7B), which appear to accurately represent what is observed in the digital color photos of exposed mouse eyes.

4.6. Pearson correlation results from interrupted recovery experiments

A Pearson correlation test showed that the mean collective lesion impact area values correlated moderately strong with exposure duration (r = 0.67; p = 0.0018), anterior chamber depth (r = −0.63; p = 0.005) and CIE L* brightness (r = 0.56; p = 0.0452). All other

variables measured were insignificant, including exophthalmia, lens opacity area, lens opacity magnitude, lens opacity integrated density, corneal thickness, and CIE a* & b* trends.

5. Discussion

Numerous adverse effects, some of which may render subjects vulnerable to unforeseen complications, have been reported in mice anesthetized with the popular mixture combination of Ketamine and Xylazine. These include hypothermia, bradycardia, hypoxia, and alteration of blood-gas tensions such as acute respiratory acidosis and hypercapnia (Arras et al., 2001; Tsukamoto et al., 2015). Retina and brain are two of the most highly metabolic organs in the entire body (Wong-Riley, 2010). Surprisingly, when performing experiments on small animals, often little or no proactive measures are used to counter these adverse effects on normal physiology of these and other tissues in the body.

In terms of vision-related complications, practically any form of general anesthesia will likely have profound effects on ocular tissues. Delicate ocular surfaces exposed to air rely heavily on eyelid function and tear film replenishment for the preservation of corneal integrity (Peng et al., 2014). Cessation of an involuntary blink reflex, which occurs rapidly with the onset of general anesthesia, means tear film depletion and corneal desiccation are imminent. Exophthalmia further exacerbates this problem as increasing palpebral space accelerates the rate at which desiccation occurs (Rolando and Refojo, 1983). Although not considered extreme, standard environmental room conditions (~25 °C & 20–45% relative humidity) found in practically all climate-controlled laboratories can still be deleterious to the eye if left exposed for a prolonged period. In addition to these visibly apparent side effects, many undesirable ocular changes have been reported in mice following KX anesthesia including reversible cataracts or media opacities (Weinstock and Scott, 1967; Calderone et al., 1986; Ridder et al., 2002; Bermudez et al., 2011; Bell et al., 2014), reduced aqueous humor production (Dugdale, 2010), reduced intraocular pressure (Ding et al., 2011), corneal damage (Turner and Albassam, 2005; Koehn et al., 2015), refractive shift (Tkatchenko and Tkatchenko, 2010), and compromised retinal and choroidal perfusion (Muir and Duong, 2011; Moult et al., 2017). As others and we (Fig. 1A and B) have shown, many of these effects are short-lived and usually reverse upon recovery; however, long-term damage can ensue.

In these studies, we have demonstrated that lesions involving the outer retina develop in two independently maintained lines of wild type mice following general anesthesia and simulated routine experimental procedures. The two recovery conditions tested demonstrate that: (1) eyes protected from desiccation using evaporation-impermeable methods (ointment + eye shield) do not result in the development of any immediate, or latent, ocular complications regardless of how the mouse is recovered (open vs. closed chambers), (2) eyes left unprotected, but insulated from the effects of evaporation accomplished by placing the mouse in a closed, humidified chamber showed only one minor complication (lens media opacities) that resolved upon recovery, and (3) eyes left exposed to the elements of circulating room air at standard environmental temperature and humidity levels exhibited substantial ocular complications, including the development of prominent outer retinal

lesions. A sigmoid curve fit of the data obtained in this study shows that the risk of developing lesions occurs around 30 min post-exposure onset and reaches a maximum probability of > 90% beyond 45 min.

The comprehensive imaging studies we performed involving both anterior and posterior poles provided probable cause as to why a lesion did or did not materialize under the different conditions tested. As anterior segment SD-OCT imaging showed, mice recovered in the open chamber without any ocular protection underwent continual change over time as the sedation cycle ran its natural course. Our original hypothesis, exophthalmia-induced lesions, was negated by observations of ocular exophthalmia in all mice regardless of ocular protection or recovery chamber status (Fig. 5C and D). Proptosis occurred soon after recumbence and remained relatively constant compared to other parameters measured post-EPIP (Fig. 6). After anesthesia induction, visible exophthalmia was observed and soon followed concomitantly by other changes such as corneal thinning, lens media opacity changes, and anterior chamber depth. Lens media opacity magnitude appears to approach a plateau first at ~15 min, followed by corneal thinning at ~20 min and lens media opacity area and integrated density at ~30 min. These changes all reached asymptotes at 25–30 min post-recumbence with exception to anterior chamber depth, which continued to change with increasing exposure time. This decrease did not seem to occur as a result of the cornea collapsing or the deflation of anterior chamber compartment. Instead, the lens steadily migrated into the anterior chamber as a result of a void being left by the loss of aqueous humor. Previous studies with KX anesthesia in mice have shown a precipitous decline in intraocular pressure over time (Ding et al., 2011), which tends to support our imaging observations of decreasing anterior chamber depth, synonymous with decreasing chamber volume. As revealed by Fig. 5A and G, lens migration was substantial as approximately half of the lenses observed came into direct contact with the posterior corneal surface. In some occurrences, the anterior lens capsule appeared to adhere to the corneal endothelium (Fig. S9-Ex. A-arrows) causing traction on the lens capsule whereby opening a void filled with semi-reflective fluid between the capsule and lens (Fig. S9-Ex. A-asterisks). At long exposure times (~1 h or more), any aqueous humor remaining within the anterior chamber became semi-reflective by anterior segment SD-OCT; presumably due to precipitated analytes, cellular infiltration, or protein flare (Fig. S9-Ex. B-asterisks). Concomitantly during this time, it could be observed that perturbations in shape and symmetry of the cornea began to appear (Fig. S9-Ex. A & B). We suspect that these anterior segment changes are substantial enough that they could be the underlying cause of corneal ulcerations and microphthalmia that commonly occur in mice following experimental studies; which occurred in 14% (3/22) of our mice left exposed in the open chamber for 65 min or longer.

Based on these observations we propose that a cascade of events leads to the formation of retinal lesions in unprotected eyes. This cascade is shown diagrammatically in Fig. 8 and is segmented into three phases of progression. First, when mice are administered anesthesia and pupil dilation drops, they receive a massive dose of alpha-1 & 2 adrenergic receptor agonists that results in vasoconstriction, extraocular muscle relaxation, and as we and others have shown, exophthalmia (Calderone et al., 1986). Soon after that, processes involved with tear film production and aqueous fluid turnover are suspected to be "clamped" or at least substantially disrupted (Calderone et al., 1986). These conditions render the eye prone to

complications, as it is unable to regulate and adequately supply or drain aqueous humor production from the ciliary bodies, Trabecular meshwork and Schlemm's canal. Drug-induced exophthalmia, causing excessive ocular exposure, results in rapid depletion of the tear film whereby corneal desiccation and dehydration ensue. As the rate of evaporation exceeds that of aqueous humor production, prolonged exposure depletes aqueous humor volume via transcorneal water loss (Weinstock and Scott, 1967; Fraunfelder and Burns, 1970). As water loss ensues, the steady reduction in anterior chamber volume is followed by a concomitant decrease in intraocular pressure. As the aqueous volume and pressure decline, we speculate that a pressure imbalance occurs between the anterior and vitreous body. The differential results in the lens being either drawn or pushed into the anterior chamber from the loss of aqueous humor or positive pressure from the vitreous body, respectively. Alternatively, exophthalmia appears to position the lens equator right at the supraorbital margins. Taking into account the decreasing anterior chamber volume and pressure, in conjunction with the marble-like rigidity of the lens, this atypical positioning arrangement of the globe may apply enough extra-orbital pressure on the superior and inferior regions to semi-extrude or propel the lens into the anterior chamber.

As exposure duration progresses, the now prolapsing ocular lens begins to apply ever-increasing tension on the radial suspensory ligaments (e.g., zonules of Zinn). The ligaments connect the lens to the inner ocular surface, inserting first at the ciliary processes, passing through the Pars plana, and terminating at the Ora Serrata (McCulloch, 1954; Shi et al., 2013). The ligaments tether the lens to the inner ocular globe surface in an entirely circumferential manner. As the lens moves farther into the anterior chamber, the tension being applied on the RPEBruch's membrane complex (RPE-BMC) exceeds the point at which some areas of the choriocapillaris can sustain perfusion, ultimately, causing localized ischemia to specific regions. The ischemia is short-lived as it is followed immediately afterwards by reperfusion upon recovery from the effects of sedation. Unfortunately, the cause and effect outlined here remain somewhat speculative since it is impossible to visualize this process in real time by *in vivo* imaging. Non-invasive imaging methods (e.g., FA, ICGA or OCT-A) that could be used to investigate this phenomenon further are not feasible due to the severe media opacities that occur during the process. Nevertheless, evidence to support this hypothesis can be found in Muir and Duong (2011), whose work demonstrated reduced perfusion in the choroids of mice anesthetized with KX vs. Isoflurane (Muir and Duong, 2011).

Imaging and histological observations have revealed that the induced damage is limited to the outer retina as no evidence of retinal vasculature or inner retina damage has been documented. The damage we have observed post-induction via non-invasive imaging appears to be specifically limited to the RPE and immediately adjacent photoreceptor layer. This observation underscores how important perfusion and oxygenation are to the metabolically demanding outer retina and RPE. The diminishing lesion visibility over time suggests that there is an initial area at risk followed by a smaller area of necrosis, much like that observed in ischemia-reperfusion injury of mouse myocardial tissue (Bohl et al., 2009). In the long-term example shown in Fig. 4, the dark area demarcated at day 3 by IRDF was suggestive of an area at risk as the visible IRDF changes disappeared by 14 days post-induction. Meanwhile, RFDF, BAF, TEFI color fundus, and FA-SLO show that perturbations

still persist at 80 days post-induction and are indicative of some lasting consequences (e.g. infarct). Between these time points the initial area of risk became an area of necrosis that was only ~75% of the original risk size. Ideally, future studies would address in more detail the dynamics between acutely visible damage and the long-term consequences of the initial brief insult observed at 3 days post-induction.

Essential to those that do not have the capabilities to screen animals using *in vivo* fundus imaging instruments, we observed an informative correlation between the media opacity color and brightness and the risk of lesion development. If the opacity is of faint brightness and has a bluish-gray hue, then our observations demonstrate that there is a low risk that a retinal lesion has formed by that particular moment. However, if the media opacity is bright, and predominantly more grayish-white in hue, then it is very likely that the retina is at risk of developing lesions. These changes appear to occur in two general phases that can be divided at ~25-min recovery mark. Under a ½ hour, during the early phase, opacity magnitude and area reach a plateau within ~25 min. At this time the reduction (~25%) in anterior chamber depth is small, and thus the lens is still quite distal from the posterior cornea. This condition gives the lens media opacity a bluish hue to the observer since the lens is still quite distal from the cornea. As we showed in Figs. 5 and 6, beyond ½ hour during the late phase the media opacity magnitude and area are no longer changing since they have reached plateaus. Still changing in the late phase, however, is the anterior chamber depth and lens position, which has now further halved the distance to the posterior cornea with 20 additional minutes elapsed by the 45 min time point. This change now places the lens within 150 μm (range ~75–200 μm) of the posterior cornea, thus causing the media opacity to lose its bluish-hue and become brighter and grayish-white in appearance. This trend continues beyond 45 min with opacities becoming brighter and slightly more white as the lens continues to approach the cornea. In summary, mice with eyes that look like white ping-pong balls have an extremely high probability of exhibiting retinal lesions.

As we demonstrated, environmental conditions during recovery can have a protective or deleterious effect on the development of retinal lesions and other ocular complications. We have demonstrated that using a humidified chamber or petrolatum-based ointment and eye shield that eyes can be protected from these undesirable occurrences with a high degree of confidence. Here, the ointment-eye shield combination served as a primary-secondary means of protection with the latter serving more as a visual indicator than an absolute necessity. If eye shields are unavailable, a simple alternative can be to apply a small square piece of saran wrap over the eye in conjunction with ointment. However, further simplifying this procedure is that in our experience a liberal blob of ointment placed alone over the eye will provide enough protection to prevent lesions and complications as long as the mice recover within a couple of hours. Yet another approach would be to hasten recovery time using reversal agents such as Atipamezole and Yohimbine, which has been shown to work in approximately 20 min post-injection following general anesthesia with KX(Mees et al., 2018). If recovery times are reliably short as demonstrated by Mees et al., (2018), then one could potentially employ viscous, aqueous-based gels and solutions like Genteal or Gonak to protect the eye. On the contrary, if recovery times are not predictably short, then lesions will be imminent in a matter of time as aqueous-based solutions will be susceptible to both evaporation and corneal absorption. Fig. 9 shows various factors that could influence the

cascade of events including transcorneal water loss, lens migration, and ischemia onset. Factors that influence dehydration and desiccation, such as air convection velocity, temperature, and relative humidity will act directly on the eye to either increase or decrease transcorneal water loss. Topically applied supplemental hydrating agents, in addition to the physical properties of those solutions, will also influence the rate of transcorneal water loss. Systemic suppression of normoxia and normothermia by general anesthesia may also play a contributing role and can be easily mitigated with supplemental heat and oxygenation. Despite these factors, the best and least complicated protection we have found comes from merely using non-volatile, petrolatum-based products that are impervious to evaporation and corneal absorption.

In this study, we provided strong evidence to show that procedure-induced retinal lesions occur in mice undergoing anesthesia induction and experimental manipulation followed by inadequate post-procedure care. These observations were supported by substantial structural and functional evidence. Lesions are most extensive within a few days of induction and appear to diminish rapidly within a few weeks of observation. Although they appear to mostly resolve, at least within the photoreceptor region, evidence of long-term consequences to the RPE persist at 2.5 months post-induction. This discovery is highlighted by the fact that these are previously undocumented observations that could be potentially useful to researchers wishing to induce transient ischemia-reperfusion injury to the outer retina of small rodents. Since the currently observable damage appears to be limited to the RPE and outer retina it is plausible that this model is unique from previously published methods used achieve retinal ischemia in mice by elevating intraocular pressure or performing arterial ligation (Buchi et al., 1991; Minhas et al., 2015; Hartsock et al., 2016). As we have shown, this model is easily reproduced and unique from previous approaches as it can be non-surgically and non-invasively induced. Additional studies to further define the kinetics involved in lesion development, maturation, and regression using both *in vivo* structural and functional assays will be informative. It will also be essential to perform additional spatiotemporal histological analyses to better identify the short and long term consequences of an ischemia-reperfusion event on the retinal tissue, namely photoreceptor and RPE cell viability.

Supplementary Material

Refer to Web version on PubMed Central for supplementary material.

Acknowledgements

References

Arras M, Autenried P, Rettich A, Spaeni D, Rulicke T, 2001 Optimization of intraperitoneal injection anesthesia in mice: drugs, dosages, adverse effects, and anesthesia depth. Comp. Med 51 (5), 443–456. [PubMed: 11924805]

Bell BA, Kaul C, Bonilha VL, Rayborn ME, Shadrach K, Hollyfield JG, 2015 The BALB/c mouse: effect of standard vivarium lighting on retinal pathology during aging. Exp. Eye Res 135, 192–205. [PubMed: 25895728]

Bell BA, Kaul C, Hollyfield JG, 2014 A protective eye shield for prevention of media opacities during small animal ocular imaging. Exp. Eye Res 127, 280–287. [PubMed: 25245081]

Bell BA, Kaul C, Rayborn ME, Hollyfield JG, 2012 Baseline imaging reveals pre-existing retinal abnormalities in mice. Adv. Exp. Med. Biol 723, 459–469. [PubMed: 22183365]

Bermudez MA, Vicente AF, Romero MC, Arcos MD, Abalo JM, Gonzalez F, 2011 Time course of cold cataract development in anesthetized mice. Curr. Eye Res 36 (3), 278–284. [PubMed: 21275518]

Bohl S, Medway DJ, Schulz-Menger J, Schneider JE, Neubauer S, Lygate CA, 2009 Refined approach for quantification of in vivo ischemia-reperfusion injury in the mouse heart. Am. J. Physiol. Heart Circ. Physiol 297 (6), H2054–H2058. [PubMed: 19820193]

Bonilha VL, Bell BA, Rayborn ME, Yang X, Kaul C, Grossman GH, Samuels IS, Hollyfield JG, Xie C, Cai H, Shadrach KG, 2015 Loss of DJ-1 elicits retinal abnormalities, visual dysfunction, and increased oxidative stress in mice. Exp. Eye Res 139, 22–36. [PubMed: 26215528]

Buchi ER, Suivaizdis I, Fu J, 1991 Pressure-induced retinal ischemia in rats: an experimental model for quantitative study. Ophthalmologica 203 (3), 138–147. [PubMed: 1775302]

Calderone L, Grimes P, Shalev M, 1986 Acute reversible cataract induced by xylazine and by ketamine-xylazine anesthesia in rats and mice. Exp. Eye Res 42 (4), 331–337. [PubMed: 3754819]

Ding C, Wang P, Tian N, 2011 Effect of general anesthetics on IOP in elevated IOP mouse model. Exp. Eye Res 92 (6), 512–520. [PubMed: 21457709]

Dugdale A, 2010 Respiratory Emergencies. Veterinary Anaesthesia : Principles to Practice Blackwell Pub, Chichester, West Sussex; Ames, Iowa, pp. 347–353.

Fraunfelder FT, Burns RP, 1970 Acute reversible lens opacity: caused by drugs, cold, anoxia, asphyxia, stress, death and dehydration. Exp. Eye Res 10 (1), 19–30. [PubMed: 5456775]

Gargiulo S, Greco A, Gramanzini M, Esposito S, Affuso A, Brunetti A, Vesce G, 2012 Mice anesthesia, analgesia, and care, Part I: anesthetic considerations in pre-clinical research. ILAR J. 53 (1), E55–E69. [PubMed: 23382271]

Hagstrom SA, Duyao M, North MA, Li T, 1999 Retinal degeneration in tulp1−/−mice: vesicular accumulation in the interphotoreceptor matrix. Invest Ophthalmol Vis Sci 40 (12), 2795–2802. [PubMed: 10549638]

Hartsock MJ, Cho H, Wu L, Chen WJ, Gong J, Duh EJ, 2016 A mouse model of retinal ischemia-reperfusion injury through elevation of intraocular pressure. J. Vis. Exp 113.

Khan KN, Mahroo OA, Khan RS, Mohamed MD, McKibbin M, Bird A,Michaelides M, Tufail A, Moore AT, 2016 Differentiating drusen: drusen and drusen-like appearances associated with ageing, age-related macular degeneration, inherited eye disease and other pathological processes. Prog. Retin. Eye Res 53, 70–106. [PubMed: 27173377]

Koehn D, Meyer KJ, Syed NA, Anderson MG, 2015 Ketamine/xylazine-induced corneal damage in mice. PLoS One 10 (7), e0132804. [PubMed: 26222692]

Krebs MP, Collin GB, Hicks WL, Yu M, Charette JR, Shi LY, Wang J, Naggert JK, Peachey NS, Nishina PM, 2017 Mouse models of human ocular disease for translational research. PLoS One 12 (8), e0183837. [PubMed: 28859131]

Mattapallil MJ, Wawrousek EF, Chan CC, Zhao H, Roychoudhury J, Ferguson TA, Caspi RR, 2012 The Rd8 mutation of the Crb1 gene is present in vendor lines of C*57BL/6N* mice and embryonic stem cells, and confounds ocular induced mutant phenotypes. Invest Ophthalmol Vis Sci 53 (6), 2921–2927. [PubMed: 22447858]

McCulloch C, 1954 The zonule of Zinn: its origin, course, and insertion, and its relation to neighboring structures. Trans. Am. Ophthalmol. Soc 52, 525–585. [PubMed: 13274438]

Mees L, Fidler J, Kreuzer M, Fu J, Pardue MT, Garcia PS, 2018 Faster emergence behavior from ketamine/xylazine anesthesia with atipamezole versus yohimbine. PLoS One 13 (10), e0199087. [PubMed: 30372437]

Minhas G, Morishita R, Shimamura M, Bansal R, Anand A, 2015 Modeling transient retinal ischemia in mouse by ligation of pterygopalatine artery. Ann. Neurosci 22 (4), 222–225. [PubMed: 26526209]

Moult EM, Choi W, Boas DA, Baumann B, Clermont AC, Feener EP, Fujimoto JG, 2017 Evaluating anesthetic protocols for functional blood flow imaging in the rat eye. J. Biomed. Opt 22 (1) 016005–016005.

Muir ER, Duong TQ, 2011 MRI of retinal and choroidal blood flow with laminar resolution. NMR Biomed. 24 (2), 216–223. [PubMed: 20821409]

Paques M, Guyomard JL, Simonutti M, Roux MJ, Picaud S, Legargasson JF, Sahel JA, 2007 Panretinal, high-resolution color photography of the mouse fundus. Invest Ophthalmol Vis Sci 48 (6), 2769–2774. [PubMed: 17525211]

Peng CC, Cerretani C, Braun RJ, Radke CJ, 2014 Evaporation-driven instability of the precorneal tear film. Adv. Colloid Interface Sci 206, 250–264. [PubMed: 23842140]

Pinto LH, Troy JB, 2008 Survey of the research opportunities afforded by genetic variation in the mouse visual system In: Chalupa LM, Williams RW (Eds.), Eye, Retina, and Visual System of the Mouse. MIT Press, Cambridge, Mass, pp. 61–69.

Rasband WS, 1997–2012 ImageJ. U. S. National Institutes of Health.

Remtulla S, Hallett PE, 1985 A schematic eye for the mouse, and comparisons with the rat. Vis. Res 25 (1), 21–31. [PubMed: 3984214]

Ridder W III, Nusinowitz S, Heckenlively JR, 2002 Causes of cataract development in anesthetized mice. Exp. Eye Res 75 (3), 365–370. [PubMed: 12384099]

Rolando M, Refojo MF, 1983 Tear evaporimeter for measuring water evaporation rate from the tear film under controlled conditions in humans. Exp. Eye Res 36 (1), 25–33. [PubMed: 6825731]

Samuels IS, Bell BA, Sturgill-Short G, Ebke LA, Rayborn M, Shi L, Nishina PM, Peachey NS, 2013 Myosin 6 is required for iris development and normal function of the outer retina. Invest Ophthalmol Vis Sci 54 (12), 7223–7233. [PubMed: 24106123]

Shi Y, Tu Y, De Maria A, Mecham RP, Bassnett S, 2013 Development, composition, and structural arrangements of the ciliary zonule of the mouse. Invest Ophthalmol Vis Sci 54 (4), 2504–2515. [PubMed: 23493297]

Thévenaz P, Ruttimann UE, Unser M, 1998 A pyramid approach to subpixel registration based on intensity. IEEE Trans. Image Process 7 (1), 27–41. [PubMed: 18267377]

Tkatchenko TV, Shen Y, Tkatchenko AV, 2010 Analysis of postnatal eye development in the mouse with high-resolution small animal magnetic resonance imaging. Invest Ophthalmol Vis Sci 51 (1), 21–27. [PubMed: 19661239]

Tkatchenko TV, Tkatchenko AV, 2010 Ketamine-xylazine anesthesia causes hyperopic refractive shift in mice. J. Neurosci. Methods 193 (1), 67–71. [PubMed: 20813132]

Tsukamoto A, Serizawa K, Sato R, Yamazaki J, Inomata T, 2015 Vital signs monitoring during injectable and inhalant anesthesia in mice. Exp. Anim 64 (1), 57–64. [PubMed: 25312399]

Turner PV, Albassam MA, 2005 Susceptibility of rats to corneal lesions after injectable anesthesia. Comp. Med 55 (2), 175–182. [PubMed: 15884781]

Weinstock M, Scott JD, 1967 Effect of various agents on drug-induced opacities of the lens. Exp. Eye Res 6 (4), 368–375. [PubMed: 6060548]

Wong-Riley MT, 2010 Energy metabolism of the visual system. Eye Brain 2, 99–116. [PubMed: 23226947]

Zeller W, Meier G, Burki K, Panoussis B, 1998 Adverse effects of tribromoethanol as used in the production of transgenic mice. Lab. Anim 32 (4), 407–413. [PubMed: 9807753]

Zweifel SA, Engelbert M, Laud K, Margolis R, Spaide RF, Freund KB, 2009 Outer retinal tubulation: a novel optical coherence tomography finding. Arch. Ophthalmol 127 (12), 1596–1602. [PubMed: 20008714]

Author Manuscript
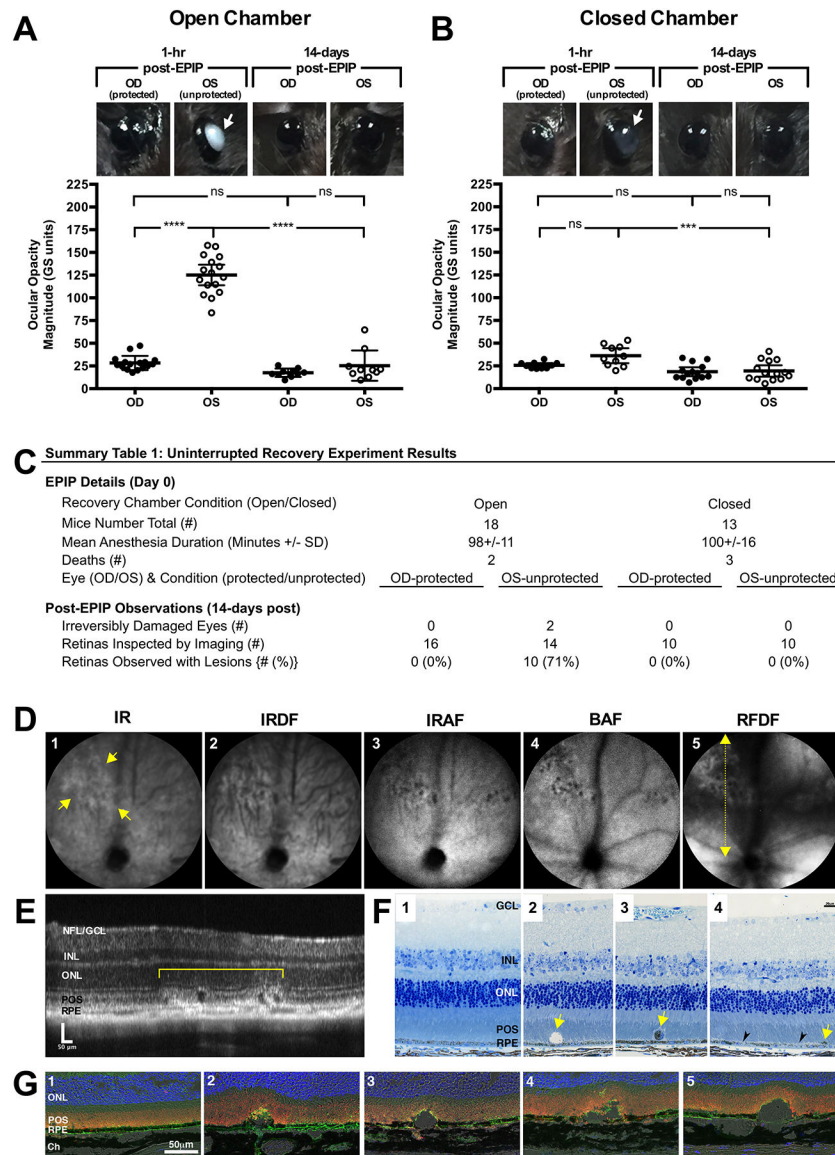
Author Manuscript

Author Manuscript

Author Manuscript

Fig. 1. Uninterrupted Recovery Experiment Results.
(**A & B**) *C57BL/6J* and *Tulp1*$^{+/+}$ mouse eyes that receive no form of ocular protection developed lens media opacities that could be visualized by the naked eye. Opacities were worse in the exposed (OS) eyes of mice recovered in the open (**A**) vs. closed (**B**) chamber at 1-hr post-EPIP. For the most part, these opacities resolved by 14-days post-recovery with exception to two instances of irreversibly damaged eyes that resulted in microphthalmia. Eyes that were covered with protective ointment and eye shields did not develop any significant lens media opacities regardless of whether the recovery chamber was open or closed. Arrows indicate the eyes with visible opacities. Note the distinctive difference in the media opacity appearance between mice recovered under high-humidity conditions vs. a typical room environment with lower humidity levels. (**C**) Experimental details and a summary table of the observations made for fundus imaging of *C57BL/6J* and *Tulp1*$^{+/+}$ mice at 14-days post-EPIP. (**D**) Representative SLO images from a *Tulp1*$^{+/+}$ mouse with retinal

lesions using IR, IRDF, IRAF, BAF, and RFDF imaging modes. Yellow arrows indicate the margins of a retinal lesion observed 14-days post EPIP recovery. RFDF (**D**; yellow dotted-line w/arrows) image indicates the approximate location of the SD-OCT B-scan shown (**E**) that was collected through an SLO detected lesion. Dark spots in BAF-SLO image are indicative of the cysts found subsequently by SD-OCT imaging (**E**) and histology (**F^2 & G$^{2-5}$**). (**F**) Photomicrographs of one regular (**F^1**) and three abnormal (**F$^{2-4}$**) thin section histology examples collected from one unaffected and three individually or affected mice, respectively. **F^2** shows an enlarged cyst-like structure above the RPE that is mostly devoid of material with exception to several pigment granules. **F^3** shows a detached, nucleated cell filled with pigment. **F^4** shows clustered pigment (yellow arrows) and hypopigmented (black arrowheads) regions of RPE. Immunohistomicrographs of one regular (**G^1**) and four abnormal (**G$^{2-5}$**) examples collected from one unaffected and four individual affected mice, respectively (Blue-TOPRO-3, Green-GLUT1, & Orange-Rhodopsin). (**G$^{2-5}$**) Subretinal cyst-like structures and disruptions to the photoreceptor outer segments and interface with the RPE are readily visible. Perturbations as large as 50 μm can be seen displacing photoreceptor inner and outer segment lamina in the vitreal direction. OCT/Histology Abbreviations: Nerve Fiber Layer (NFL), Ganglion Cell Layer (GCL), Inner Nuclear Layer (INL), Outer Nuclear Layer (ONL), Photoreceptor Outer Segments (POS), Retinal Pigment Epithelium (RPE), and Choroid (Ch).
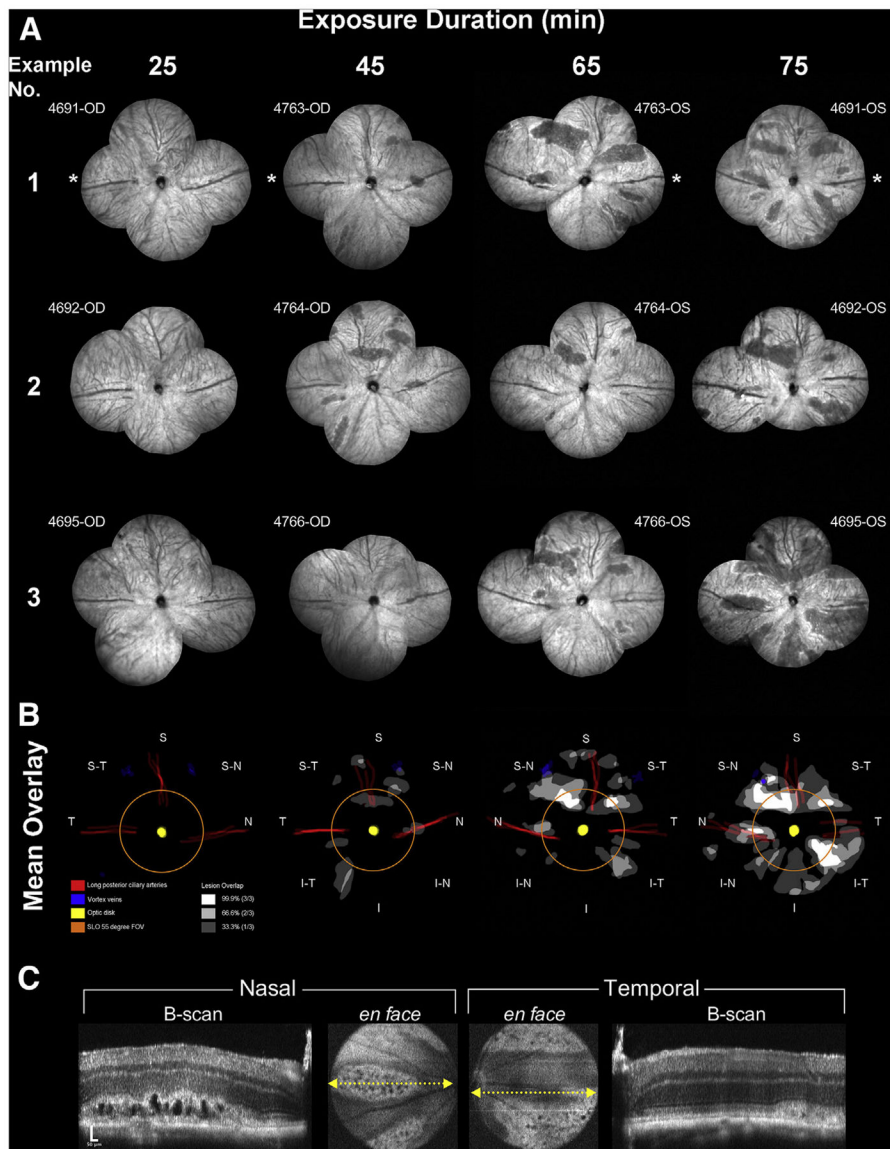
Fig. 2. Montaged fundus views and results from the interrupted exposure time point experiments.

The extent of the induced abnormalities at 3 days post-EPIP can be seen in three examples provided for each interruption time point (**A**). These examples represent 12 individual eyes from 6 *Tulp1*$^{+/+}$ mice. Asterisks indicate the temporal region. No abnormalities are visible at 25 min whereas the number and size of the lesions can be seen increasing with more prolonged exposure duration. Lesion involvement overlays were created for each retina example that also included demarcating the location of the vortex veins, optic disk, and long posterior and superior ciliary arteries. Mean overlays of lesion involvement were created to identify lesion development hot spots related to retinal quadrant (**B**). As observed, lesions occur in various regions of the posterior pole and in particular, within specific lanes or zones within those regions. The orange ring shows the extent of FOV for the SLO 55° wide-field lens. Note that many lesions form outside this central retina FOV, which is reasonably conserved among commercially available color fundus, SLO and SD-OCT imaging

instruments capable of imaging mice. (**C**) SD-OCT images from the horizontal meridian of the mouse (#4695-OS) from Fig. 2A IRDF-SLO example #3 @ 75 min Post-EPIP recovery time showing the prominent formation of large vacuoles or cyst-like structures within the photoreceptor layer.
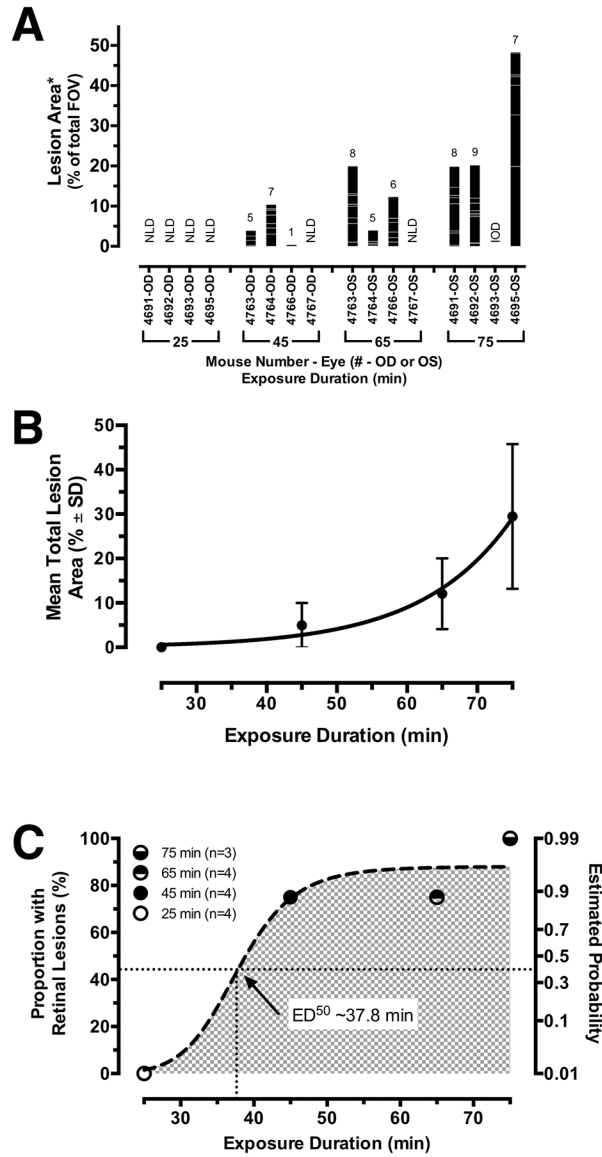
Fig. 3. - Quantified Results from the Interrupted Experiments.

(**A**) Data obtained from the IRDF-SLO images shown in Fig. 2A of eyes that underwent interrupted recovery protection at 25, 45, 65, and 75 min post-EPIP. A stacked bar graph indicates eyes from *Tulp1*^{+/+} mice (n = 8) exhibiting lesions (columns) along with the numbers of individual lesions counted (number of stacked intracolumn bars; total # provided above column), the areas of each individual lesion (individual intracolumn bar height), and the collective areas of all individual lesions observed per eye (column height). Abbreviations: NLD-no lesions detected, IOD-irreversible ocular damage. (**B**) The mean total lesion area for affected eyes (mean ± SD.) fitted with an exponential growth curve (Adjusted R^2 = 0.98). (**C**) Effective dose time-response curve generated from the proportion of eyes found with lesions and the estimated probability of retinal lesions. This trend underscores that eyes cannot be left unprotected for more than ½ hour before the risk of developing retinal lesions begin. Note that the curve is steep and shows that the mice

transition from moderate (50%) to high risk (> 90%) within 10 min beyond the ½ hour exposure mark.
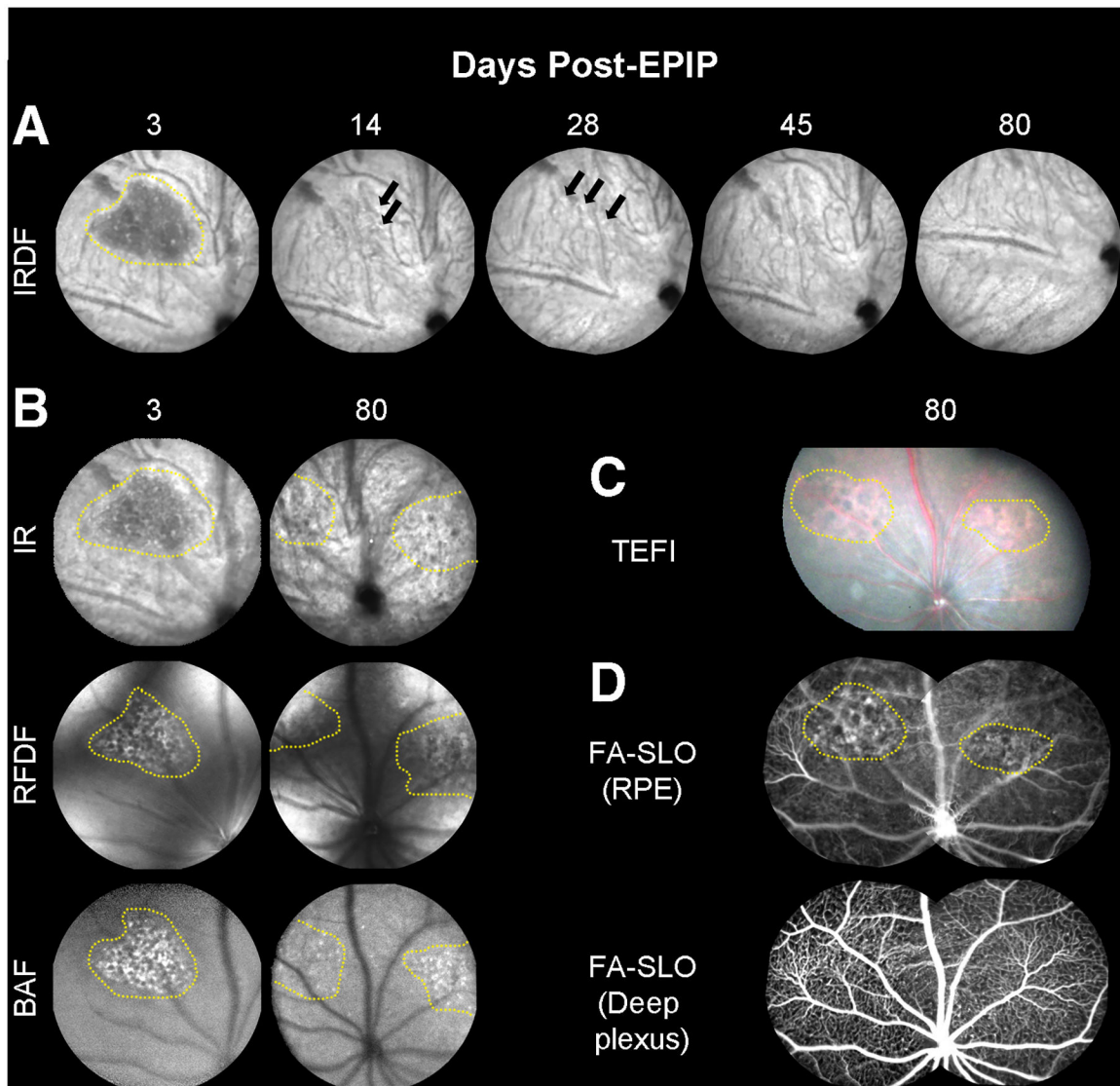
Fig. 4. Long-term follow up of retinal lesions.

(**A**) Representative IRDF-SLO images of lesions in a *C57Bl/6J* mouse at 3-days post-EPIP, which are easily discernable from the standard RPE/choroidal background (n = 3)… The lesion is presented as a dark region that has resolved 14-days post-EPIP. At 14 and 28-days, subtle indicators (hyper- and hypo-reflective spots) persist that suggest some evidence of the lesion remains. By 45 and 80-days, the hyper- and hypo-reflective perturbations have resolved, and the region appears similar to the surrounding background. (**B**) Additional examples of the same lesion shown by IRDF (Fig. 4A) at 3-days post are also readily visible by three of the other SLO imaging modes (IR, RFDF, and BAF). This comparison helps to identify and isolate the region impacted by the lesion, which appears to be the outer retina and RPE. As a result of this observation, it is suggestive that the lesion remaining at 80 days post-EPIP is also altered RPE and this is further supported by the TEFI and FA-SLO images that follow. (**C**) Color fundus images showing a different spectral reflectance profile for the two visible lesions versus the surrounding background. (**D**) Sodium Fluorescein

Angiography (FA-SLO) revealing leakage or abnormal uptake of the fluorophore at the RPE level whereas no evidence of leakage can be observed in the deep plexus of the retinal vasculature. The enhanced visualization of red reflectance and green fluorescence for the TEFI and FA-SLO images, respectively, could alternatively be due to hypo-pigmentation of the RPE as previously indicated in Fig. 1F[4]. These observations suggest that the damage remaining at this late stage is isolated to the RPE.
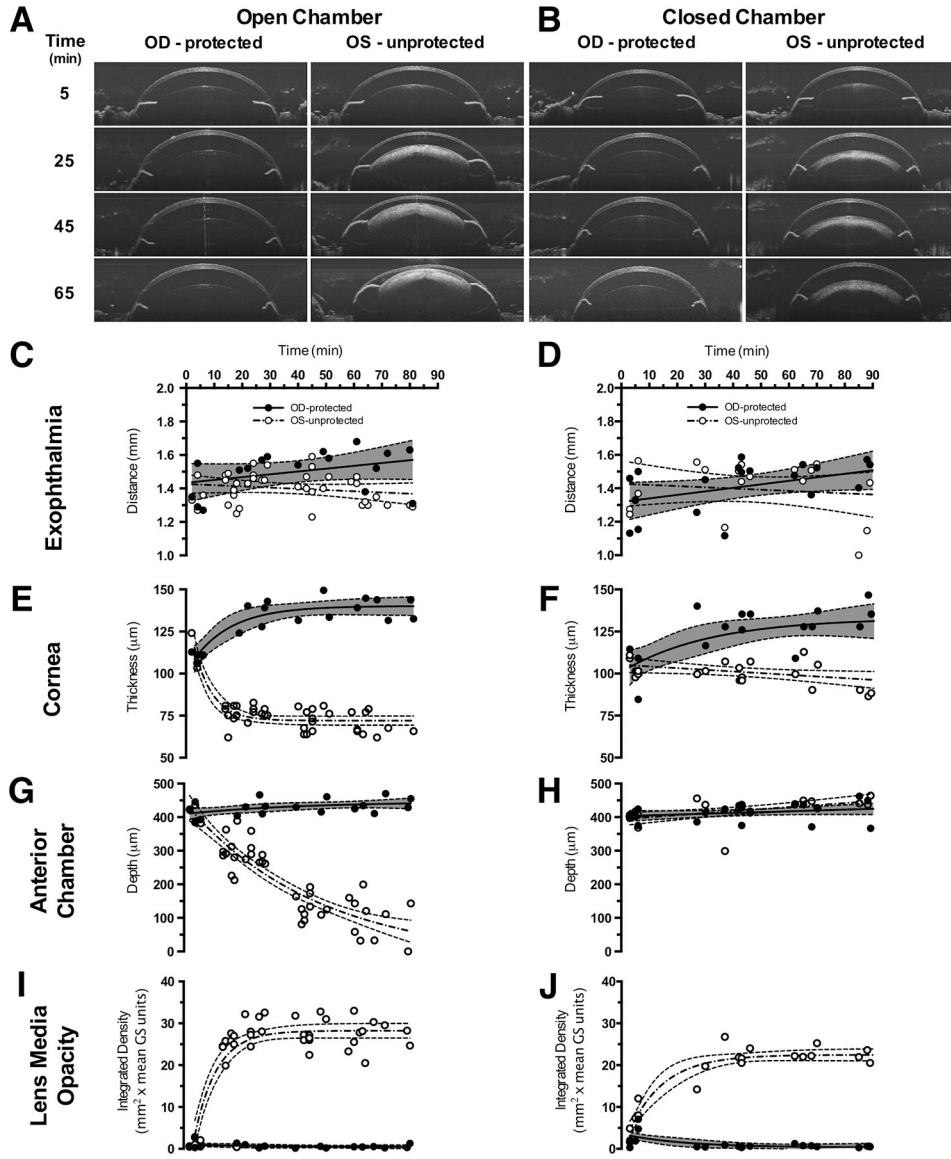
Fig. 5. Anterior Segment SDOCT Imaging Examples and Quantified Results
Representative SDOCT images from the anterior segment of *Tulp1*$^{+/+}$ mice (n = 8) recovered in the open (**A**) vs. closed (**B**) chambers. Eyes of mice that received ocular protection **(OD-protected)** exhibited no substantial adverse changes compared to eyes that were left unprotected **(OS-protected)**. However, mice with unprotected eyes **(OS-unprotected)** and recovered in the closed chamber (**B**) only developed lens media opacities in contrast to mice with unprotected eyes **(OS-unprotected)** and recovered in the open chamber that (**A**) developed visibly apparent corneal thinning, lens media opacities and reduction in anterior segment depth. Quantitative results for exophthalmia (**CD**), corneal thickness (**E-F**), anterior chamber depth (**GH**) and lens media opacity (**I-J**) for the two ocular status and two recovery and conditions.
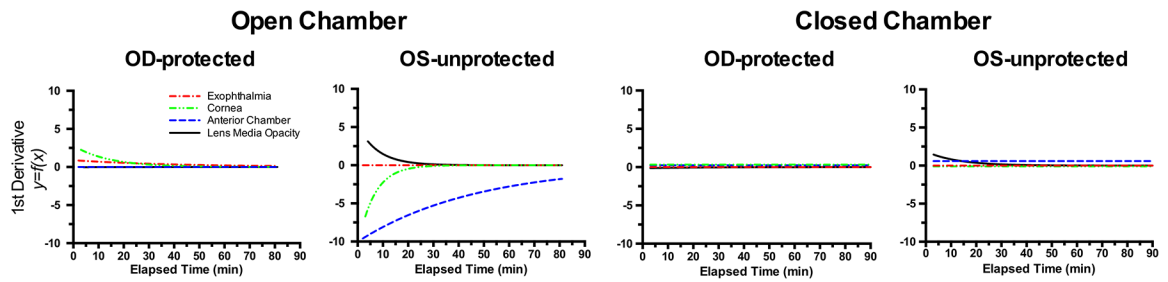
Fig. 6. Rate of Change Comparisons

First derivatives taken of the fitted curve trends shown in Fig. 5 reveal the rate of change for exophthalmia, corneal thinning, anterior chamber depth collapse, and ocular lens media opacity development. These curves show the magnitude, direction, and rate of change associated with these metrics measured *in vivo* via anterior segment SD-OCT imaging. Note that the most prevalent changes occur in the unprotected left eyes (**OS-unprotected**) of mice that are recovered in the open chamber. Furthermore, anterior chamber depth is observed having the largest magnitude and most sustained rate of change during the 80 min of monitoring.
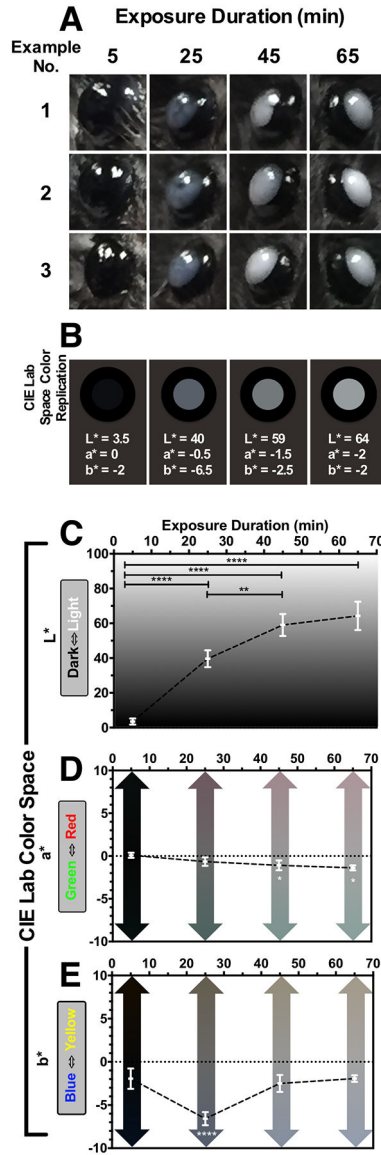
Fig. 7. Changes in Ocular Appearance with Exposure Duration

(**A**) Three examples of media opacities observed in *Tulp1*$^{+/+}$ from mouse eyes (n = 8) at 5, 25, 45, & 65 min post-EPIP. Qualitatively, it is easily observed that eyes immediately following EPIP have a charcoal black appearance and transition to a bluish-gray hue within 25 min. Past 25 min, eye opacities become brighter in appearance and proceed towards a neutral, grayish-white color. These visual, qualitative observations were quantified so that they could be shown graphically in CIE L*a*b* color space (**C-E**). (**C**) Brightness (L*) significantly increased with exposure duration. (**D**) Green-Red (a*) exhibited a small (~2–3 units), but significant shift from neutral to a green hue after 45 and 65 min. (**E**) Blue-Yellow (b*) experienced a slightly larger (5 units) and very significant shift (p < 0.0001) to blue at 25 min from the original neutral black color at 5 min. Moreover, at 45 & 65 min post-EPIP, the blue hue found at 25 min significantly returned to the original baseline value observed at 5 min. Color values obtained for the plots shown in **C-E** were used to generate a CIE Lab

Space Color Rendition **(B)** to recreate the mean appearance of mice with ocular opacities artificially. In these examples, the mean CIE Lab values for the pupil are reported as L*, a*, b* values and displayed in a two-dimensional, en face view of the mouse eye including the surrounding iris and periorbital region. This example demonstrates that the reconstituted color values are similar to the *in vivo* digital color photographic observations and accurately replicate these changes. Retinal lesion impact area correlated moderately strong with ocular exposure duration, decreasing anterior chamber depth and opacity brightness. Thus, it would appear that opacity brightness is an excellent visual indicator of lesion development probability.
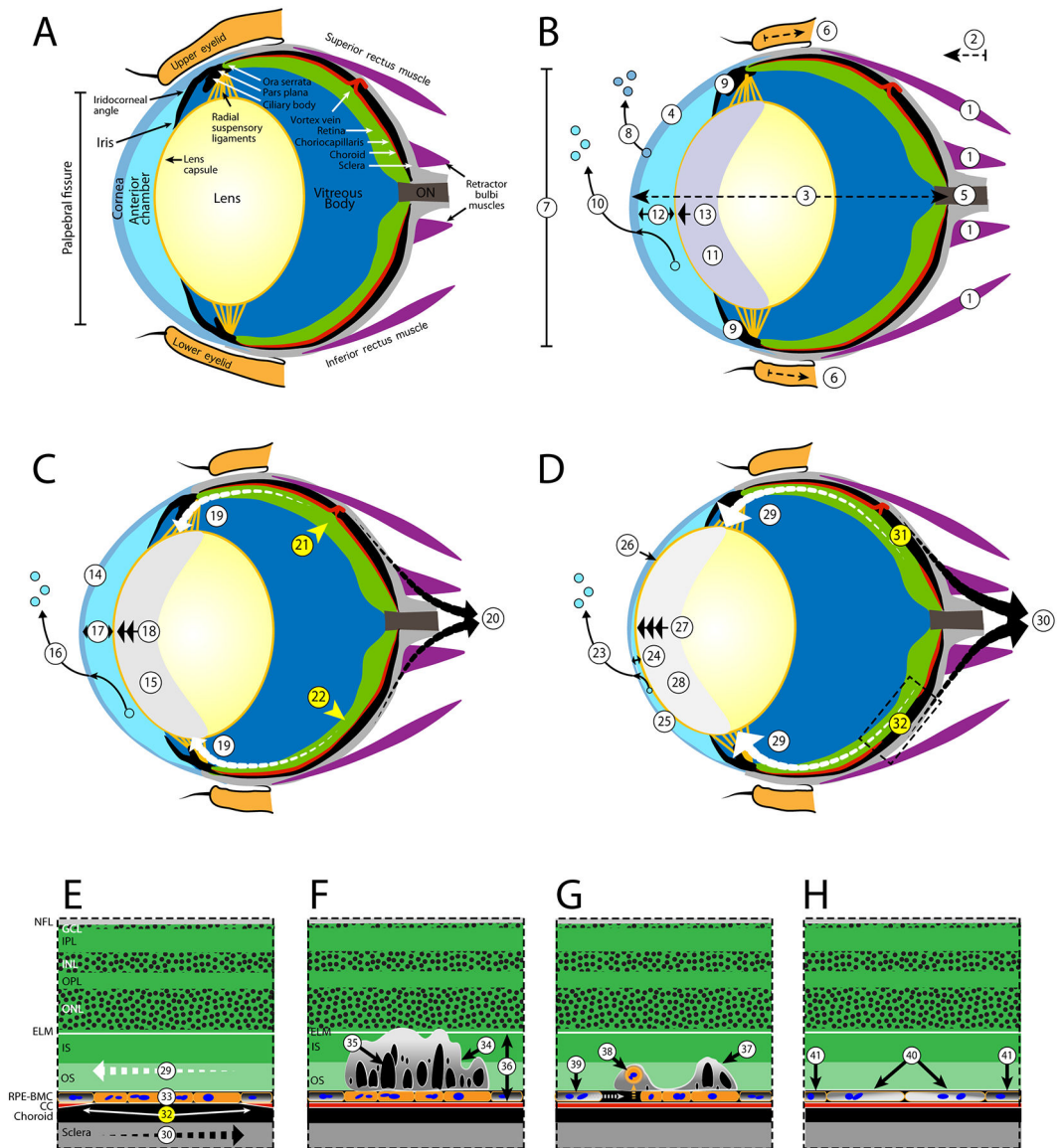
Fig. 8. Etiology of Procedure Induced Retinal Lesions in Mice

Suspected processes leading to mechanically induced ischemia (**A-D**) and the latent development of outer retinal lesions (**E-G**) in a normal mouse eye. For ischemia development, the changes are divided into three periods (**B-D**) that describe early (< 20 min), mid (20–40 min), and late (40 + min) time frames. For lesions, the earliest record of their presence at 3-days post-EPIP is demonstrated (**E**). Lesions do substantially regress over time as depicted by 14- and 80-days post-recovery illustrations (**FG**). **A. Normal eye** - Schematic of a normal adult mouse eye, modified from Remtulla and Hallett (1985) and Tkatchenko et al., (2010), detailing the anatomical regions and features suspected to be impacted post-EPIP. Note: the vortex vein is shown in the incorrect anatomical position for purposes of demonstrating stenosis and pinch-occlusion in the mid and late time phases, respectively. **B. Early phase** - General anesthesia and mydriasis induction with xylazine and phenylephrine result in adrenergic agonist activation and systemic changes that include

smooth muscle relaxation, vasoconstriction, decreased perfusion, hypoxia, hypercapnia, bradycardia, respiratory acidosis, hypothermia, etc. (changes not depicted). Immediately post-EPIP, extraocular muscles become relaxed (**1**), causing exophthalmia (**2**), globe elongation (**3**), modified corneal curvature (**4**), increased load on the optic nerve (**5**), retraction of the eyelids and cessation of blink reflex (**6**), widening of the palpebral fissure (**7**), and rapid depletion of corneal tear film (**8**). Aqueous humor production and outflow via the ciliary bodies and Schlemm's canal are reduced (**9**) followed by transcorneal loss of aqueous humor (**10**) and development of lens media opacity that persists until full recovery from sedation (**11**). A reduction in aqueous humor volume results in decreasing anterior chamber depth (**12**) followed by migration of the ocular lens (**13**) into the chamber. Extraocular pupillary appearance observed at this time has a faint bluish-hue due to lens media opacity formation (**11**). **C. Mid phase** Asymptotic limits for corneal desiccation and thinning (**14**) are reached followed by lens media opacity magnitude, area and integrated density (**15**). Extraocular pupillary appearance transitions from bluish-gray to grayish-white due (**15**). Sustained loss of aqueous humor via transcorneal evaporation (**16**) leads to additional reductions in anterior chamber volume/depth (**17**) and lens prolapse (**18**). Lens prolapse applies tension on the radial suspensory ligaments, Ciliary bodies, Pars Plana, Ora Serrata and RPE-BMC (**19**). Opposing forces between the RPE-BMC (**19-white arrows**) and the choroid (**20-black arrows**) induce an inner vs. outer laminar strain and impede blood perfusion via mechanically-induced stenosis of the vortex veins (**21**) and choriocapillaris (**22**). Lesion development probability approaches 50% during the mid-phase period. **D. Late phase** - Prolonged desiccation to the exposed eye assures that retinal lesions and other ocular complications are imminent. Evaporative fluid loss continues to deplete aqueous humor volume (**23**), further decreasing anterior chamber depth (**24**), resulting in a misshapen cornea (**25**), occasionally causing lens misalignment and resulting in the risk of adhesion to the corneal endothelium (**26**). A 3-to 4-fold change in lens prolapse (**27**) gives the pupil a bright white appearance (**28**) and applies increasing tension on the radial suspensory ligaments, the Ciliary bodies, Pars Plana, Ora Serrata and RPE-BMC (**29**). Estimated probability (~51–95%) for lesion development occurs from 39 to 55 min post-EPIP as increasing shear occurs between RPE-BMC (**29-segmented tapered white arrows**) and the choroid (**30- segmented tapered black arrows**) increases severity of the ischemic regions (**31–32**) that involve either pinch-occlusion of a vortex vein (**31**) or regional mechanical-induced stenosis of the choriocapillaris (**32**). **E. Expanded FOV of Ischemia Affected Area** - Opposing forces acting along the RPE-BMC (**29**) and choroid (**30**) mechanically collapse the choriocapillaris (**32**) causing an ischemic episode contributing to anaerobic stress to the RPE (**33**). Upon recovery from sedation, all various ocular systems aforementioned return to normal and the choriocapillaris undergoes reperfusion (not shown). Abbreviations: Nerve Fiber Layer (NFL), Ganglion Cell Layer (GCL), Inner Plexiform Layer (IPL), Inner Nuclear Layer (INL), Outer Plexiform Layer (OPL) Outer Nuclear Layer (ONL), External Limiting Membrane (ELM), Photoreceptor Inner (IS) and Outer Segments (OS), Retinal Pigment Epithelium & Bruch's Membrane complex (RPE-BMC), and Choriocapillaris (CC). **F. 3-Days Post-EPIP** - Three days following recovery, prominent retinal lesions are viewable via fundus imaging and indicate areas that previously underwent ischemia-reperfusion injury post-EPIP. A cross-sectional view illustrates the characteristics of a lesion when observed at this time point using SD-OCT imaging. Lesions involve the IS

and OS laminar structures of the photoreceptor layer and show some displacement of the ELM (**34**). Numerous subretinal cysts (**35**) are visible within the impacted lamina (**34**). RPE cells outside the ischemia-affected region are presumably normal (**36**), as outer retina lamina appear normal outside the affected regions. **G. 14-Days Post-EPIP** - Fourteen days following recovery, lesions show evidence of resolving and become more difficult to discern by fundus imaging. SD-OCT shows an area of involvement less pronounced than that observed at 3-days post-EPIP. However, a displaced photoreceptor layer containing sub-retinal features presents containing smaller and less numerous cysts (**37**). Histological evidence suggests that RPE cells encountered enough stress to become apoptotic and undergo detachment from Bruch's membrane (**38**). Detached cells undergo phagocytosis (**38**) and removal followed by expansion of adjacent RPE cells to cover the exposed area (**39**). **H. 80-Days Post-EPIP** - Imaging evidence indicates that prominent outer retinal disruptions observed at 3-days post-EPIP are 99% resolved following 2.5 months of recovery. However, imaging data also suggest that the RPE remains compromised by the original insult and is morphologically different from adjacent, unaffected regions. Remaining or adjacent RPE cells, which underwent expansion to cover exposed areas of cell loss, exhibit altered melanosome or melanin granule pigment density (**40**) compared to normal RPE cells from unaffected regions (**41**) and suggest impaired melanogenesis or altered melanodistribution in RPE cells affected by the ischemia-reperfusion injury.
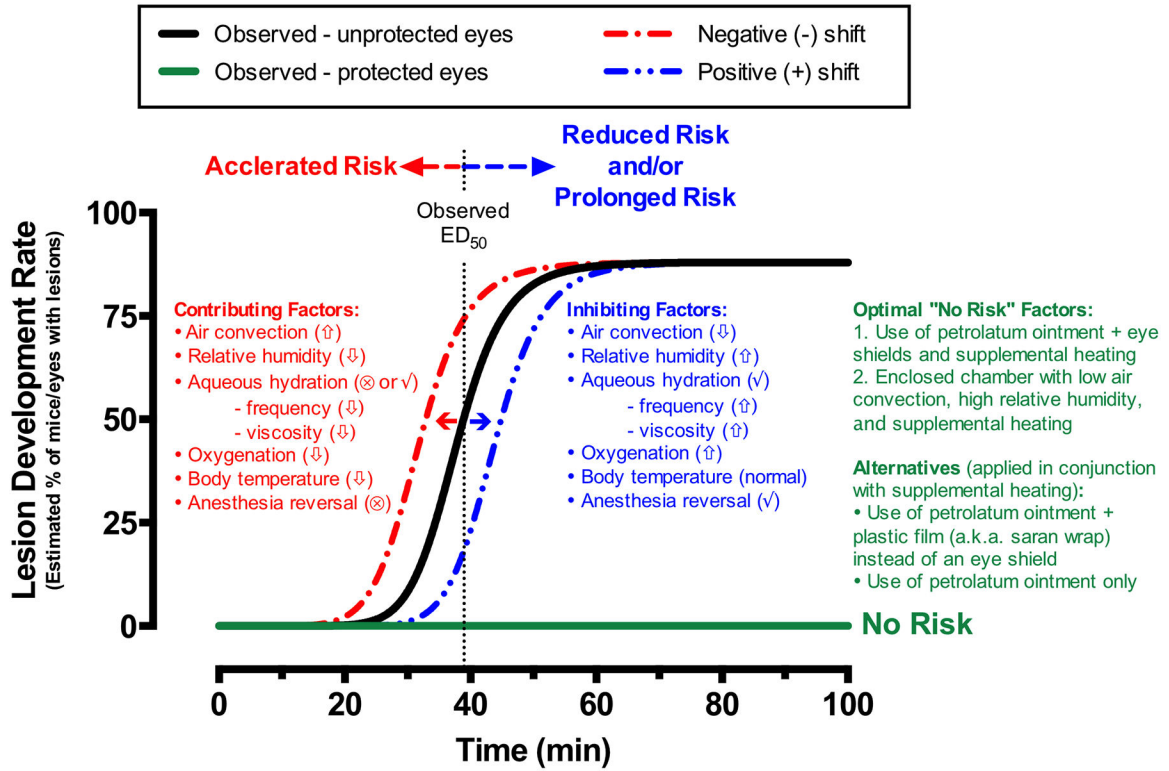
Fig. 9. Variables and Risk Factors Influencing Lesion Development

Dose-response trends established for the development (black line sigmoid trend) or non-development (flat green line) of procedure-induced retinal lesions in this study. The rate at which the cascade of events shown to transpire in Fig. 8 can influence the chances of lesion development and will depend on many factors that can either accelerate (faster onset) or reduce, but also prolong (delayed onset), the risk of developing retinal lesions. Contributing and inhibiting factors listed can induce negative or positive shifts in the dose-response trend to either increase or decrease susceptibility to this cascade of events that can lead to ocular complications. In sum, protect the eye with a non-volatile, petrolatum-based agent and use an anesthesia-reversing agent, supplemental heat and oxygen if possible to minimize the local and systemic effects of experimental procedures involving general anesthesia, mydriasis induction, and extended post-procedure recovery from sedation. Sign key: High (up arrow), Low (down arrow), and provided (✓) or not provided (⊗).